PAPER

Check for updates

Oxygen vacancy-induced ferroelectric effect in (111) strontium titanate single crystals controls photoelectrochemical water oxidation

Samutr Assavachin, [ID] Chengcan Xiao, Hamed Vahdatvasei, Tatiana Mamani, [ID] Davide Donadio [ID] and Frank E. Osterloh [ID] *

Ferroelectric materials, such as tetragonal $BaTiO_3$, have a permanent electric polarization that can be controlled with an external electric field, however, a ferroelectric polarization in cubic $SrTiO_3$ is forbidden by the higher symmetry of the lattice. Here we demonstrate that hydrogen annealed $SrTiO_{3-x}$ single crystals can be polarized electrically, and that the polarization controls the activity for photoelectrochemical water oxidation, a pathway to solar hydrogen fuel. Specifically, it is observed that the anodic water oxidation photocurrent increases from 0.99 to 2.22 mA cm^{-2} at 1.23 V RHE (60 mW cm^{-2}, UV illumination) or decreases to 0.50 mA cm^{-2} after electric polarization of hydrogen-annealed (111) $SrTiO_{3-x}$ single crystals in forward or reverse direction. The polarization also modifies the surface photovoltage signal of the material and its flat band potential, based on Mott–Schottky measurements. These observations are attributed to the formation of an electric dipole at the (111) $SrTiO_{3-x}$ surface, which alters the potential drop across the depletion layer at the solid–liquid junction, and with it the electron transfer barrier. Density functional theory calculations confirm that an electric dipole can result from the movement of oxygen vacancies between the surface or sub-surface layers of $SrTiO_{3-x}$. The filling of these surface oxygen vacancies is the probable cause for the observed disappearance of the electric polarization after 24 h storage in air and 48 h in argon. Overall, this work establishes a new surface-based ferroelectric effect in $SrTiO_{3-x}$ and its use for solar energy conversion during photoelectrochemical water oxidation. Because oxygen vacancy defects are common, similar electric polarization effects are to be expected in other metal oxides.

Broader context

Ferroelectric materials retain a permanent electric polarization after exposure to an electric field. In $BaTiO_3$, this polarization promotes photocatalytic hydrogen evolution by helping to separate photogenerated charge carriers. In the related $SrTiO_3$ a ferroelectric polarization is forbidden by the high symmetry of the cubic perovskite crystal structure. Here we show that oxygen vacancies introduced into $SrTiO_{3-x}$ single crystals by thermal annealing in a hydrogen atmosphere lower the symmetry and allow the material to become ferroelectric. When $SrTiO_{3-x}$ is employed as a photoelectrode for oxygen evolution from water, the ferroelectric polarization controls the photocurrent and the photovoltage. This occurs because the electric dipole enhances or diminishes the band bending at the semiconductor-liquid junction, depending on the dipole orientation. This is confirmed independently with surface photovoltage spectroscopy and with Mott–Schottky measurements, which show a polarization-dependent flatband potential. DFT calculations suggest that the electric dipole is tied to the movement of oxygen vacancies between surface and sub-surface layers of $SrTiO_{3-x}$. These findings show for the first time that an oxygen vacancy-induced ferroelectric effect can improve the photoelectrochemical water oxidation reaction, an important step in solar energy conversion. Similar enhancements can be expected in other metal oxides, where oxygen vacancies are common.

Introduction

Ferroelectric (FE) materials exhibit a spontaneous internal electric polarization that can be reversed through application

Department of Chemistry, University of California, Davis, CA 95616, USA.
E-mail: fosterloh@ucdavis.edu

of an external electric field.[1–4] When the FE effect is present in semiconductors, as in so-called photoferroics,[2] it can result in improved separation of photogenerated electrons and holes. This is of interest for improved photovoltaic devices and photocatalysts for the overall water splitting reaction.[5–9] Illuminated $BiFeO_3$ photovoltaic cells, for example, produce open-circuit voltages of up to 16 V,[10,11] which is known as anomalous
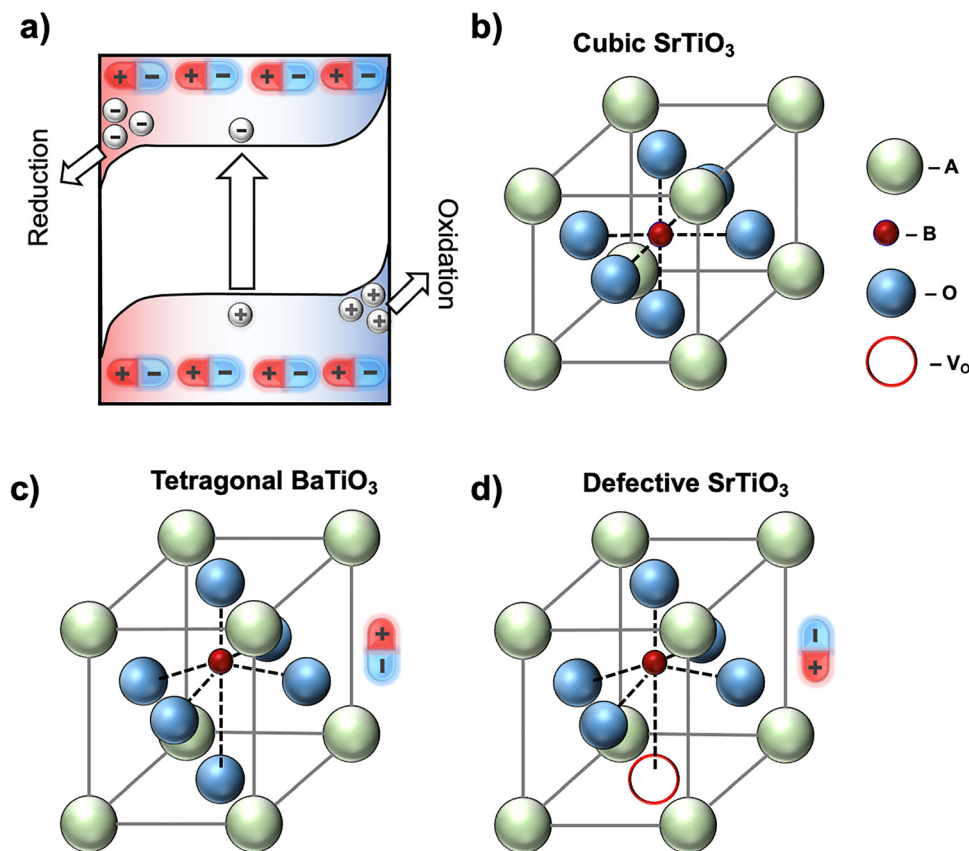
Fig. 1 (a) Ferroelectric polarization affects band bending in a photovoltaic junction. The slope of the band edges represents the built-in field (E_{bi}). From ref. 32 (b) cubic strontium titanate unit cell in cubic ABO_3 perovskite structure (A = Sr^{2+} B = Ti^{4+} O = O^{2-}). (c) Tetragonal barium titanate unit cell (A = Ba^{2+}, B = Ti^{4+}, O = O^{2-}).[33] (d) Defective strontium titanate unit cell, containing one oxygen vacancy (red circle). Dipole orientations are also shown.

photovoltaic effect (APE). As we and others showed recently, the photoelectrochemical water oxidation properties of $BaTiO_3$ can be controlled with a ferroelectric dipole at the solid–liquid interface.[12–15] Generally, in order to be a ferroelectric, a material must not crystallize in a centrosymmetric space group, because the high symmetry is inconsistent with an electric dipole. For example, while the tetragonal form of $BaTiO_3$ in Fig. 1 is ferroelectric (Curie temperature 110–120 °C),[16] the high-temperature cubic phase is not.[17–19] Interestingly, recent experimental evidence and theoretical calculations suggest that room temperature ferroelectricity in cubic $SrTiO_3$ and other centrosymmetric materials may be induced by crystal lattice distortions resulting from defects or mechanical strain. For example, ferroelectric behavior in cubic $SrTiO_3$ has been predicted theoretically as a result of the introduction of oxygen vacancies[20–22] or Frenkel defects.[23] Defect-induced ferroelectric properties were also reported recently for $SrTiO_3$ after doping with Sn,[24] Ca,[25] Pr,[26] Fe,[27] and Cr[28] and for $BiVO_4$ after doping with Na and Mo.[29] Additionally, $SrTiO_3$ thin films grown on $GdScO_3$ (110) or $DyScO_3$ substrates exhibit room-temperature ferroelectric polarization as a result of the tensile distortion induced by the substrate.[30,31] Despite these findings, to date it not clear if the defect-induced ferroelectric effect can improve the solar energy conversion of a material.

To address this question, we studied here the photoelectrochemical water oxidation properties of (111) terminated $SrTiO_3$ single crystals after the introduction of oxygen vacancies. We find that prior exposure of the material to an electric field perpendicular to the surface changes the photovoltage and photocurrent of the $SrTiO_{3-x}$/electrolyte contacts. This is attributed to a defect-induced ferroelectric effect at the surface. When the material is stored in argon atmosphere, the FE enhancement is retained for over 24 hours, but in air it disappears in less than one day. Based on X-ray photoelectron spectroscopy (XPS), the electric polarization is not associated with observable chemical changes in the $SrTiO_{3-x}$ surface region. We therefore attribute the polarization to the migration of positively charged oxygen vacancies between the surface and sub-surface $SrTiO_{3-x}$ layer in the applied electric field. This mechanism is supported by density functional theory (DFT) calculations, which show a strong dependence of the surface dipole on the position of the oxygen vacancy. Overall, these results provide the first demonstration that a defect-induced surface ferroelectric effect can improve photoelectrochemical energy conversion with a metal oxide semiconductor. The finding may be widely applicable, considering the frequent use of oxygen-defective metal oxides as photoelectrodes for water splitting.

Results and discussion

The SrTiO$_3$ single crystals chosen for this study were 1.0 × 1.0 cm^2 × 0.5 mm in size and are terminated by two (111) facets (Fig. 2a–c). Optical absorption spectra of the crystals (Fig. 2d) reveal an absorption edge at 390 nm (3.2 eV) consistent with the known 3.2 eV optical bandgap of strontium titanate.[34] In order to make the material conductive, crystals were annealed in a 10% H$_2$/90%(vol) Ar atmosphere for 5 hours at 1050 °C.[34] The hydrogen treatment causes reduction of some Ti^{4+} ions, as shown in eqn (1) in the Kröger–Vink notation.[35–37] To maintain a charge balance in the lattice, the reduction is accompanied by the formation of positively charged oxygen vacancies (eqn (2)).

$$H_2 + 2Ti_{Ti}^{\times} \rightarrow 2Ti'_{Ti} + 2H^+ \tag{1}$$

$$2H^+ + O_O^{\times} \rightarrow V_O^{\bullet\bullet} + H_2O \tag{2}$$
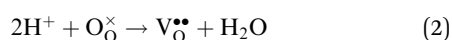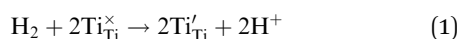
During the hydrogen treatment, the crystals turn from clear transparent to grey-black and develop a broad optical absorption in UV visible spectra (Fig. 2d). This absorption is due to excitation of free electrons in the SrTiO$_{3-x}$ conduction band.[38] Additionally, a weak absorption at 510 nm can be attributed to the $^2T_{2g} \rightarrow {}^2E_g$ transition of Ti^{3+} in an octahedral environment.[39] These changes agree with previous observations in the literature and confirm the presence of Ti^{3+} and oxygen vacancies.[40–45]

The photoelectrochemical (PEC) water oxidation properties were assessed by placing the SrTiO$_{3-x}$ crystal into a three-electrode cell, consisting of a Pt counter electrode, a calomel reference electrode, and an aerated 0.5 M Na$_2$SO$_4$ aqueous solution (pH = 5.95), as shown in Fig. S1a. A chopped light photoelectrochemical scan was conducted under 60 mW cm^{-2} ultraviolet light from a Xe lamp. As can be seen in Fig. 3a, the SrTiO$_{3-x}$ sample produces an anodic photocurrent at applied potentials positive of −0.20 V RHE. The current is stable over the course of one hour (Fig. S2) and is accompanied by the formation of a gas at the working electrode (Fig. S3).

This suggests that the current is due to oxygen evolution from water oxidation. Based on a repeat experiment under 375 nm LED illumination (Fig. S4 and Table S5) the external quantum efficiency is 52.69% at 1.23 V RHE. This value is comparable to a previous study.[46] Overall, it is known that the water oxidation efficiency of SrTiO$_{3-x}$ is limited by electron–hole recombination at oxygen vacancy induced Ti^{3+} defects[47] and by the lack of a water oxidation cocatalyst.[48]

In order to observe the effect of a prior electric polarization on the photoelectrochemical behavior of SrTiO$_{3-x}$, the hydrogen-annealed crystal was exposed to an electric field. For this, the crystal was sandwiched between two 2.0 × 4.0 cm^2 gold coated glass slides using two insulating Muscovite Mica sheets (∼65 μm thick each, details in Fig. S1b). The sandwich was then placed inside of an argon gas purged glass tube and a DC voltage of 545 V was applied across the two gold slides for one hour (1 h). Based on the thickness of the stack (0.050 cm + 2 × 0.0065 cm), the effective
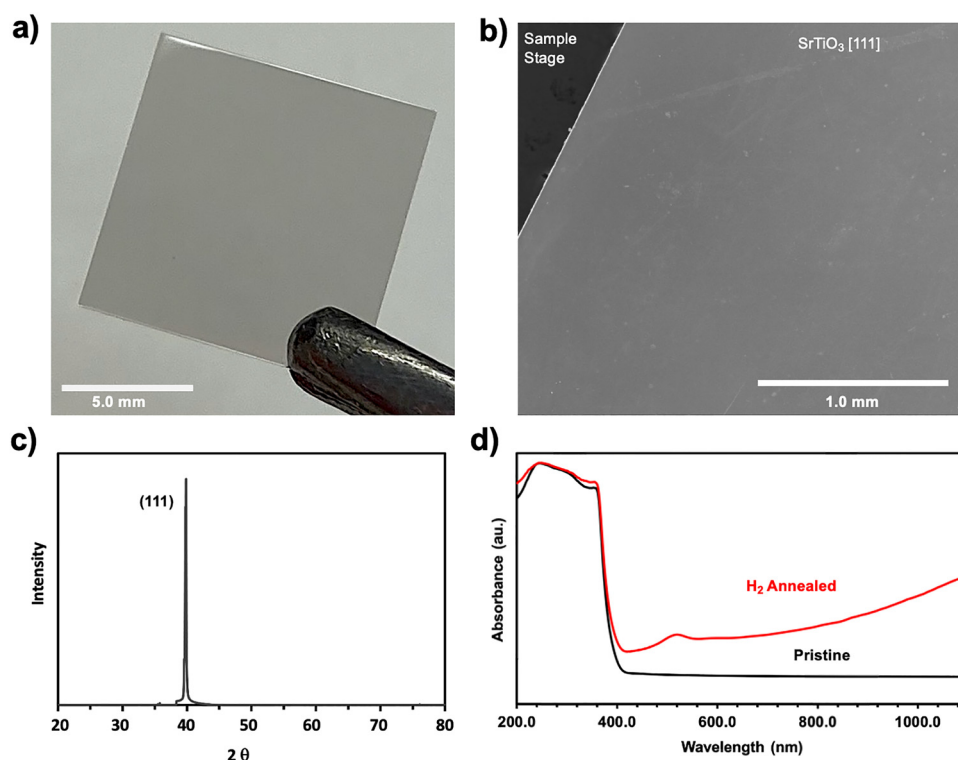

Fig. 2 (a) Photo of (111) SrTiO$_3$ single crystal, as purchased. (b) SEM image of SrTiO$_3$ single crystal surface after H$_2$ annealing. (c) XRD Pattern of H$_2$ annealed SrTiO$_{3-x}$ single crystal, confirming the (111) orientation (d) Optical absorbance spectra before and after H$_2$ annealing.
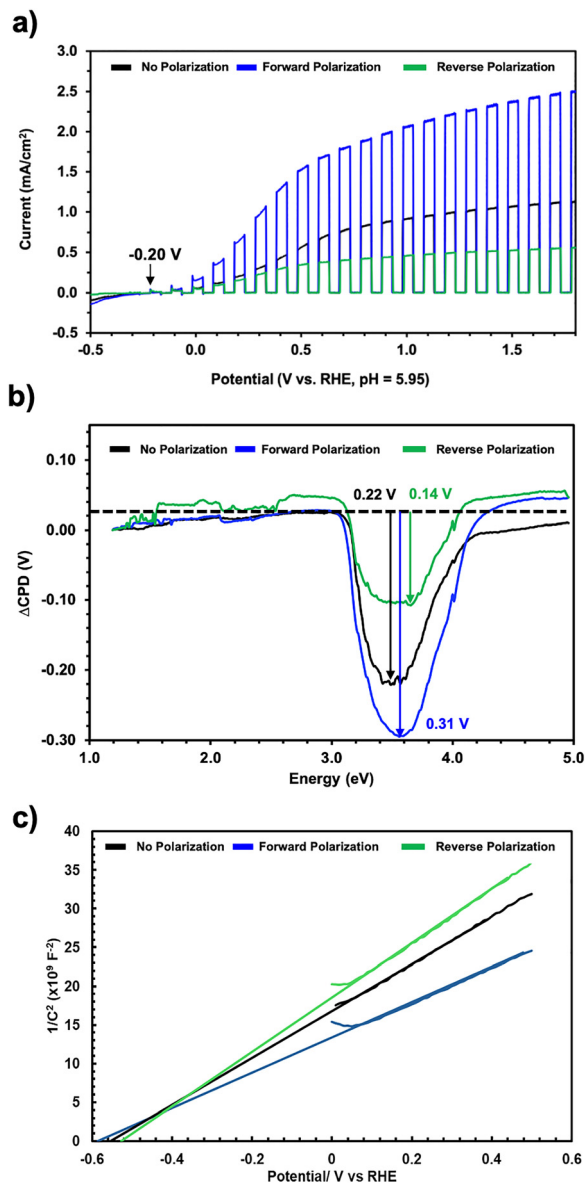
Fig. 3 (a) Chopped light linear sweep voltammetry scan of SrTiO$_{3-x}$ in 0.5 M Na$_2$SO$_4$ (aq, pH = 5.95) under 300 W Xe lamp UV light illumination (60 mW cm^{-2}). Scans were conducted from negative to positive applied potential. The crystal was contacted with InGa eutectic, as shown in Fig. S1a, to establish an Ohmic contact. (b) Surface photovoltage spectra of SrTiO$_{3-x}$ in contact with 15 μL deionized water. The SPV signal reaches its maximum value at 3.4−3.6 eV and then decays to zero above 4.0 eV due to the diminishing intensity of the light source (Xe Lamp). (c) Mott Schottky measurement of SrTiO$_{3-x}$ crystals in 0.5 M Na$_2$SO$_4$ aqueous solution with 50 mM equimolar K$_{3/4}$[Fe(CN)$_6$] (air free). During MS experiments, the exposed electrode area was ~1 cm^2. Additional Mott−Schottky plots are shown in Fig. S8.

electric field acting on the SrTiO$_{3-x}$ crystal was 8.65 kV cm^{-1}. 30 minutes after polarization, the photoelectrochemical properties of the crystal were evaluated under the same conditions as before. The PEC response for a forward polarized crystal (electrolyte-exposed crystal surface was at positive electrode during polarization) is shown in Fig. 3a (blue line). The anodic current again begins at −0.20 V vs. RHE, but now

reaches 2.22 mA cm^{-2} at +1.23 V RHE, 2.2 times the previous value. A separate PEC experiment in Fig. S4 establishes an IPCE of 71.4% at 375 nm (at +1.23 V RHE). The PEC measurement for a reverse polarized crystal (electrolyte-exposed crystal surface was at negative electrode during polarization) is also shown in Fig. 3a (green line). For this crystal the current reaches only 0.50 mA cm^{-2} at 1.23 V RHE (IPCE 48.8% at 375 nm), which is 1.99 times lower than what is found for the non-polarized crystal. This shows that forward and reverse polarization changes the anodic photocurrent of SrTiO$_{3-x}$ by a factor of ~2 relative to the non-polarized state. The effect is reproducible with other H$_2$ annealed (111) SrTiO$_{3-x}$ crystals, as shown in Fig. S6 and Table S7. On average, the photocurrent increases by a factor of 1.83 ± 0.45 or decreases by a factor of 1.93 ± 0.49 for forward and reverse polarization, respectively.

The differences in the photoelectrochemical activity can be explained with the energy diagram in Fig. 4. The SrTiO$_{3-x}$/electrolyte contact forms a Schottky-type junction that under illumination repels electrons from the liquid interface.[46,49] When the electric polarization is applied before the PEC experiment, it creates an electric dipole near the SrTiO$_{3-x}$ surface, which shifts the Flatband potential E_{FB} (the Fermi level of the non-contacted SrTiO$_{3-x}$ surface), and the band edge positions E_{CB} and E_{VB} by an amount P [V]. This modifies the built-in potential V_{Bi} of the depletion layer, given by the difference of E_{FB} and E^0. Because the built-in potential V_{Bi} creates an electrostatic barrier that prevents electrons from reaching the electrolyte, it controls the rectifying properties of the junction and its photocurrent. This is analogous to what was observed recently with ferroelectric BaTiO$_3$ nanocrystals.[12]

To further assess the effect of the surface dipole on photochemical charge separation at the SrTiO$_{3-x}$/electrolyte contact, surface photovoltage spectra (SPV) were collected using a vibrating Kelvin probe (measurement configuration in Fig. S1c).[50,51] The surface photovoltage is strictly defined as the light-induced change of the surface potential, and is measured experimentally as SPV = CPD(light) − CPD(dark),[52] where CPD is the contact potential difference between the sample and the gold Kelvin probe. As can be seen in Fig. 3b, all samples generate a negative SPV signal near 3.15 eV when the photon energy reaches the optical bandgap of SrTiO$_{3-x}$. The negative SPV signal is caused by photoholes reaching the SrTiO$_{3-x}$/liquid interface and electrons moving to the back contact (Fig. 4). As can be seen from the data, the SPV signal increases in the direction of reverse polarized < non-polarized < forward polarized SrTiO$_{3-x}$. This trend is consistent with the model in Fig. 4, i.e. the larger the band bending, the larger the photovoltage.

Further support for the model can be gained from measurements of the flatband potential, E_{FB}. E_{FB} equals the voltage bias required to remove the band bending at the SrTiO$_{3-x}$/liquid junction.[53] E_{FB} is important because it determines the potential drop V_{bi} in the depletion layer according to $V_{bi} = E_{FB} - E^0$, where E^0 is the solution redox potential. To determine E_{FB}, Mott–Schottky measurements were conducted under exclusion of air in 0.5 M Na$_2$SO$_4$ aqueous solution containing equimolar
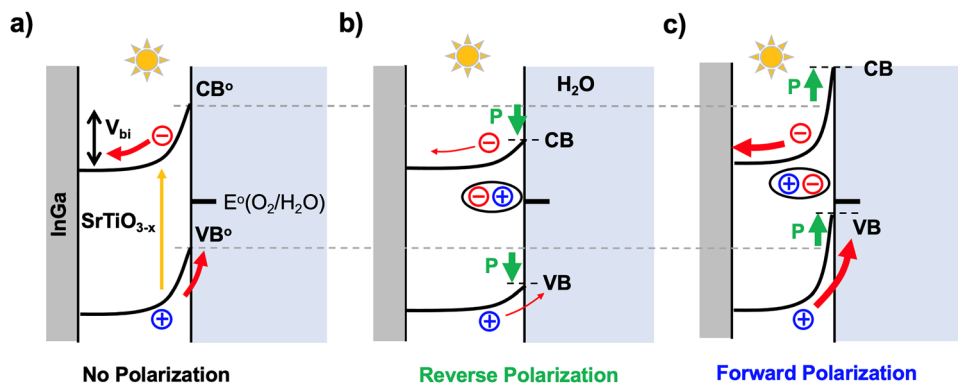
Fig. 4 Proposed band bending diagram for the SrTiO$_{3-x}$/liquid junctions during PEC water oxidation. (a) before polarization, (b) after reverse polarization, (c) after forward polarization. The electric dipole shifts band edges and Flatband potentials, depending on the dipole orientation. This controls the built-in voltage, V_{Bi}, $i.e.$ the electrostatic barrier that prevents electrons from reaching the electrolyte. CB^0 and VB^0 denote the conduction and valence band edges before polarization.

amounts of $K_3[Fe(CN)_6]$ and $K_3[Fe(CN)_6]$. The hexaferrocyanide redox couple was chosen because its charge transfer is fast,[54] promoting the formation of a depletion layer in SrTiO$_{3-x}$.

Mott Schottky plots were obtained at 20, 50, 100, 200, and 500 Hz AC frequency and are summarized in Fig. S8, with a representative plot at 100 Hz shown in Fig. 3c. Positive slopes are observed for all crystals as expected for depleted n-type semiconductors. Based on six different measurements for each crystal (data summarized in Table S9), values for the flatband potentials are -0.637 ± 0.035 V $vs.$ RHE for forward polarized crystals, -0.590 ± 0.037 V $vs.$ RHE for non-polarized crystals, and -0.5745 ± 0.031 V $vs.$ RHE for reverse polarized samples. This is an important confirmation of the model in Fig. 4, which predicts an impact of the ferroelectric polarization not just on the photocurrent, but also on the flatband potential E_{FB}. According to the experimental slopes, the electron donor concentration of the crystals varies from 1.98×10^{19} to 1.52×10^{19} and 0.23×10^{19} cm^{-3}. However, this variation is not a result of the polarization, but a result of slow surface oxidation of the crystals over the course of the measurements which took several days to complete. This is confirmed by a plot of the donor concentration $versus$ time in Fig. S10.

Based on the E_{FB} variation in the Mott Schottky plots, the polarization-induced flatband shift P has a mean value of 31 mV. Theoretically, one would expect this variation to affect the water oxidation photo-onset potentials in Fig. 3a, however, this is not observed. This appears to be a consequence of the small size of the flatband variation. Additionally, it is known that oxygen has a strong Fermi level pinning effect in SrTiO$_3$, which can mask the influence of the FE polarization on the photo-onset potential.[43,55]

Next, in order to determine the lifetime of the FE polarization in SrTiO$_{3-x}$, chopped-light LSV scans were repeated 24 h and 48 h after the initial electric field application. According to Fig. 5 the polarization effect disappears completely within a 24 h interval for samples stored in air, but is retained longer for samples stored in argon atmosphere. For example, in argon, 100% of the FE enhancement obtained from forward
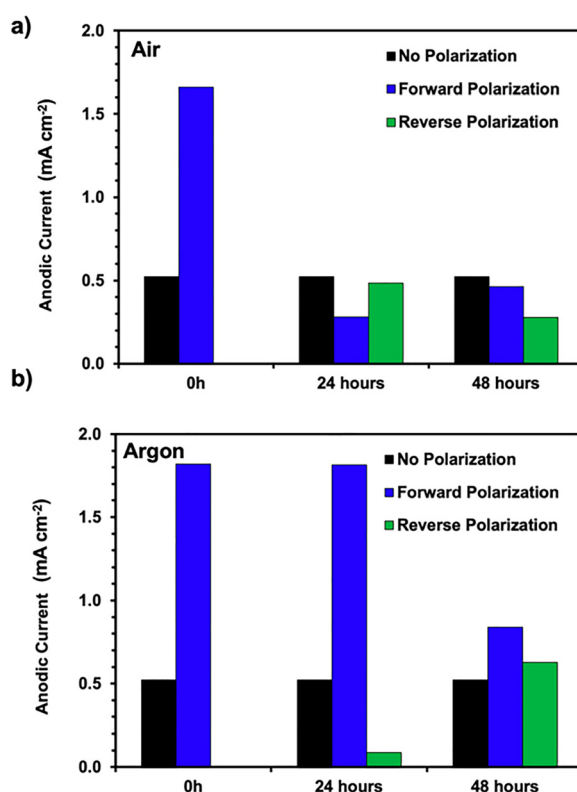

Fig. 5 PEC water oxidation photocurrent at 1.23 V RHE at the indicated times after initial polarization. (a) Sample storage in the dark in air, (b) sample storage in the dark under argon flow.

polarization is present after 24 h and 53% after 48 h. Similarly, 83% of the FE suppression from reverse polarization is retained after 24 h but disappears after 48 h. This confirms that the polarization effect is air-sensitive, as observed in the Mott Schottky data, and possibly involves the removal of oxygen vacancies at the SrTiO$_{3-x}$ surfaces, during air storage or during photoelectrochemical water oxidation.

To better understand the effect of the electric polarization on the surface chemistry of SrTiO$_{3-x}$, X-ray photoelectron
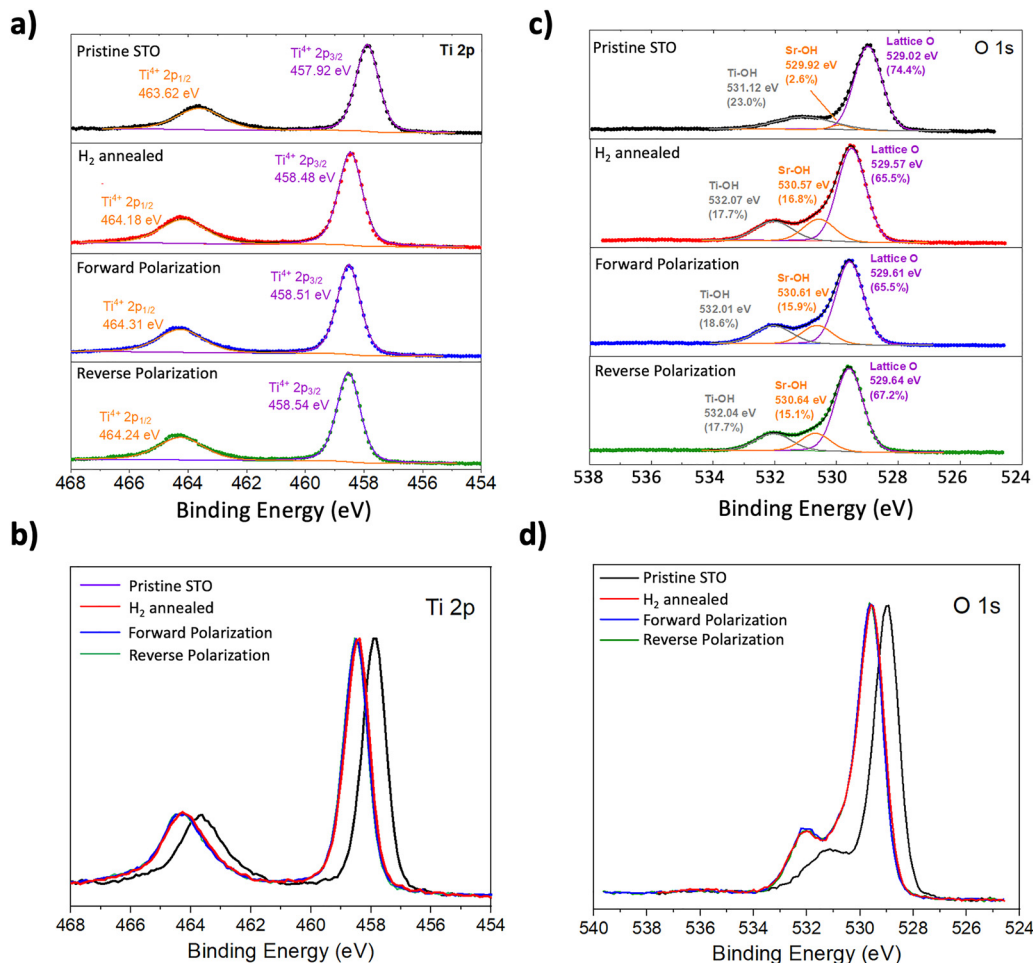
Fig. 6 (a) Peak fit and (b) overlap of the Ti 2p spectra of pristine SrTiO₃ (purple), H₂-annealed SrTiO₃₋ₓ without polarization (red), with forward polarization (blue) and reverse polarization (green), respectively. (c) Peak fit and (d) overlap of the O 1s spectra.

spectroscopy (XPS) was employed. High-resolution data for the Ti and O regions is shown in Fig. 6 and additional data and survey spectra are shown in Fig. S11 and S12 and in Table S13. For the pristine SrTiO₃ (as-purchased) single crystals, the Sr 3d₅/₂ peak at 132.42 eV, Ti 2p₃/₂ peak at 457.90 eV and O 1s peak at 529.02 eV match the results from previous works.⁵⁶⁻⁶⁰ All Ti atoms are found in the +4 oxidation state, and all O atoms in the −2 oxidation state. The two O 1s peaks are assigned to lattice O and surface OH groups, respectively. After H₂ annealing, a binding energy shift towards higher energy for all three elements was detected, suggesting a Fermi level shift toward more reducing potentials. This is evidence of an increase in free electron density in SrTiO₃₋ₓ (see earlier discussion in Zhao et al.⁴⁷). Based on the 0.55 eV shift for Ti 2p₃/₂ (457.92 to 458.48 eV) and O 1s (529.02 eV to 529.57 eV), and the slightly larger shift of 0.61 eV for Sr 3d₅/₂ (132.42 to 133.02 eV), the average Fermi level change in SrTiO₃₋ₓ is 0.58 eV.

Surprisingly, no Ti³⁺ was detected, which can be attributed to the small penetration depth of XPS (5 nm) and the effect of air oxidation, as observed previously.⁴³ Surface Ti³⁺ ions formed during the H₂ annealing treatment undergoes air oxidation to Ti⁴⁺ with concomitant formation of hydroxide. The hydroxide

gives rise to a new O 1s peak at 530.6 eV in Fig. 6c, which is assigned to surface Sr–OH hydroxide species according to the work by Hrabovsky and co-authors.⁵⁸ The remaining two oxygen peaks at 529.57 eV and 532.07 eV are assigned to lattice O and surface Ti–OH, respectively.

Survey and high-resolution XPS spectra for SrTiO₃₋ₓ measured within the first hour after forward and reverse polarization are shown in Fig. S11 and S12, respectively. No significant changes in the relative intensity and peak positions were found after these treatments. However, when high resolution Ti spectra are overlaid in Fig. 6b, a 0.04–0.07 eV Fermi level shift relative to non-polarized SrTiO₃₋ₓ is evident. This Fermi level shift is much smaller than after H₂ annealing (0.58 eV) and occurs in the direction of higher energy, regardless of polarization direction. We attribute it to the removal of surface water during the one-hour polarization treatment of the SrTiO₃₋ₓ crystals in dry argon atmosphere.

Importantly, the XPS data shows that electric polarization is *not* associated with significant changes in the chemical surface composition of the SrTiO₃₋ₓ wafer. This rules out electrosegregation of ions at the SrTiO₃ surface as the cause of the local polarization. Such a process was previously observed for
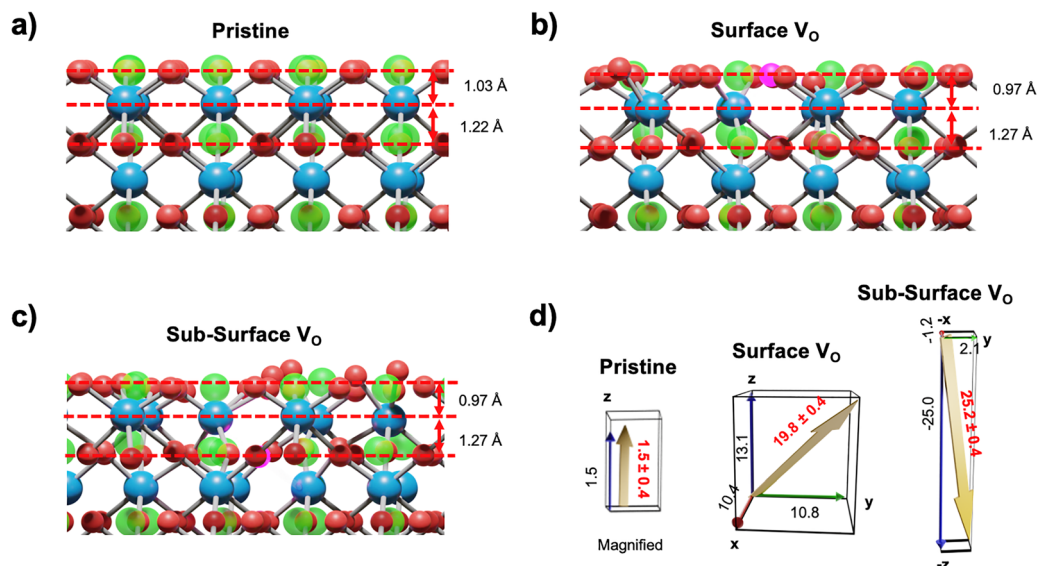
Fig. 7 Calculated structures for the pristine (111) $SrTiO_3$ surface (a) before and after the introduction of a (b) surface oxygen vacancy (pink spheres) or a (c) sub-surface oxygen vacancy. Ti ions are shown as blue spheres and Sr ions as green spheres. (d) Calculated electric dipole density [D/nm²] is represented by arrows (pointing from negative to positive charge).

$La_{0.1}Sr_{0.9}TiO_3$ during electric polarization at high temperature (1000 °C),[61] where the ion mobility is much increased.

To explain the ferroelectric effect in room temperature polarized $SrTiO_{3-x}$, we hypothesize that the electric field moves oxygen vacancies in the sub-nanometer surface region of $SrTiO_{3-x}$. To test this idea, the local structure and dipole density of a 3-unit cell thick $SrTiO_{3-x}$ slab was computed with DFT with Hubbard corrections (DFT+U).[62,63] Calculated structures of the (111) $SrTiO_{3-x}$ before and after introduction of oxygen vacancies are shown in Fig. 7. The model for the pristine V_O-free $SrTiO_3$ crystal (calculated unit cell dimensions of 3.977 [Å]) agrees well with crystallographic data (3.905 Å)[64,65] from the literature (Table S14). The calculated DOS diagram in Fig. S15 is also similar to a previous report.[47]

The initial 3-unit-cell thick $SrTiO_{3-x}$ slab (111) is terminated with SrO_3 layers on both surfaces, leading to an ideally zero net polarization when the atoms occupy their crystallographic positions. All Ti^{4+} ions are in their expected octahedral O_6 environments with Sr^{2+} ions occupying voids between the TiO_6 octahedra. Once the atoms of the top surface are allowed to relax (the positions of the bottom surface are constrained), the $SrTiO_{3-x}$ slab in Fig. 7a undergoes a slight compression of the top Ti–O layer (1.03 A) relative to the buried Ti–O layers (1.03 A). The movement of the O^{2-} ligands toward Ti^{4+} ions generates a surface dipole (yellow arrow in Fig. 7d) with the indicated polarity (positive charge outside and negative charge inside the slab). The dipole is normal to the surface, as the in-plane symmetry is not broken, but it exhibits small finite x and y components that reflect the uncertainty of the calculation. Structural changes resulting from the removal of one surface oxygen atom, which corresponds to a surface density of 0.42 vacancies per nm², are shown in Fig. 7b. We note that in order to achieve convergence of the calculation, two electrons

needed to be added to the slab, which, however, remains p-type based on the DOS in Fig. S15. The Bader charge analysis in Fig. S16 shows that the charge redistribution upon vacancy formation and addition of two electrons occurs mostly among the surface oxygen atoms, leaving the charged states of Ti and Sr unchanged. This is in contrast to previous calculations on bulk $SrTiO_{3-x}$, which favor localization of the excess electron density in the two undercoordinated Ti^{3+} ions near the oxygen vacancy site.[47] As can be seen from Fig. 7b, the addition of the surface O vacancies shrinks the distance between the surface and subsurface layers from 1.03 to 0.97 A, and increases the distance to the layer underneath to 1.27 A. This produces a surface dipole density of 19.8 ± 0.4 D nm^{-2}, over one order of magnitude larger than without the vacancy (Fig. 7d). The dipole density is aligned with the excess positive charge in the Sr–O surface layer, where the vacancy was formed, and an excess negative charge in the layers below. Significant x and y components of the dipole are also observed, which are attributed to the distorted geometry of the TiO_5 polyhedron and to the motion of the surrounding O^{2-} and Sr^{2+} ions towards the vacancy.

A very different picture arises when the O vacancy is generated in the sub-surface layer (Fig. 7c). Since now the positive charge of the vacancy appears below the layer of surface Ti ions, the resulting dipole inverts its sign (positive charge inside the slab and negative charge outside), as shown in Fig. 7d Additionally, the dipole in is increased in magnitude to 25.2 ± 0.4 D nm^{-2}, which is the result of substantial restructuring of Sr^{2+} and O^{2-} ions in the sub-surface layer.

Overall, the DFT calculations confirm the dependence of the surface dipole on the oxygen vacancy position and the role of restructuring in generating x and y components in the dipole density. Importantly, the calculated dipole densities in Fig. 7

can explain the observed ferroelectric effect in polarized $SrTiO_{3-x}$ crystals. As mentioned in eqn (1) and (2), the oxygen vacancies in $SrTiO_{3-x}$ carry a positive charge while the Ti^{3+} ions are negatively charged. These charged species will experience a mechanical force in an electric field.[66] Forward polarization (when the positive electrode is on the $SrTiO_{3-x}$ surface) moves positively charged O vacancies into the sub-surface layer, away from the surface, corresponding to a negative electric dipole pointing out of the surface. This dipole enhances the band bending at the solid–liquid junction, as shown in Fig. 4 and improves the photoelectrochemical water oxidation performance of the $SrTiO_{3-x}$ crystal. Reverse polarization has the opposite effect. Here, positively charged O vacancies move to the surface layer, creating a positive dipole pointing out of the surface. This dipole reduces the potential drop across the junction and its water oxidation performance, as shown in Fig. 4. Therefore, the DFT model in Fig. 7 is in good agreement with the dipole model in Fig. 4.

Earlier DFT calculations have estimated the activation energy for oxygen vacancy movement as 0.14 eV.[67] This energy value is easily achieved with the high electric field (8.65 kV cm^{-1}) during the one-hour polarization treatment. This confirms the electric field-driven oxygen vacancy migration at the $SrTiO_{3-x}$ surface as a possible source of the ferroelectric effect in $SrTiO_{3-x}$. Indeed, many recent works show that oxygen vacancies can migrate and modify the electric properties of surfaces and interfaces. Oxygen vacancy migration has been identified as cause for photocurrent onset switching in 300 nm $Bi_{0.9}Sr_{0.1}FeO_3$ films,[68] and in $BiFeO_3$ single crystals,[69] and in 2.5–9 nm thin ZrO_2 films[70] and in Cr-doped $SrTiO_3$ films.[71] According to Jiang *et al.*, oxygen vacancies in $SrTiO_3$ have mobilities of 1.5×10^{-13} cm^2 V^{-1} s^{-1} at room temperature and in an electric field of 500 kV cm^{-1},[72] and can be manipulated with a Kelvin probe force microscopy tip[73] *via* a process called 'resistive switching'.[74]

The surface oxygen vacancy migration model for $SrTiO_{3-x}$ also explains the limited stability of the effect in air, where O_2 can react readily with $SrTiO_{3-x}$ to fill oxygen vacancies at the surface. This is well established in the literature.[67] This reactivity may limit the longevity of the defect-induced FE effect in photoelectrochemical water oxidation applications, unless means to protect the $SrTiO_{3-x}$ surface can be found. Interestingly, the observed FE enhancement in $SrTiO_{3-x}$ appears quite comparable to that in tetragonal $BaTiO_3$ nanocrystals, a true ferroelectric.[12] There, forward polarization at 52.8 kV cm^{-1} also causes a two-fold increase of the photocurrent, and the polarization effect also disappears after storing samples in air for 3 days. Because repeat photoelectrochemical tests are central to these experiments, it is possible that the harsh conditions during water photoelectrolysis are to blame for the polarization disappearance. Further measurements are needed to evaluate this hypothesis.

facets induce a surface ferroelectric effect that can be controlled with an applied electric field. Electric polarization in the forward direction (positive electrode on $SrTiO_{3-x}$ surface) increases the water oxidation photocurrent under UV light nearly two-fold [1.83 ± 0.45 (24.6%) at 1.23 V *vs.* RHE] while reverse polarization suppresses it by a factor of two [(1.93 ± 0.49) (25.4%)]. Surface photovoltage data confirm the improved or diminished photochemical charge separation for polarized samples. These findings can be explained with a junction model that assumes that the band bending at the $SrTiO_{3-x}$/liquid interface is modified by a ferroelectric surface dipole. The dipole effect is verified experimentally with Mott Schottky measurements, which reveal a shift of the flatband potential by 30 mV to more reducing or oxidizing values. Although the polarization effect disappears within 24 h in air, argon storage extends its lifetime to 48 hours. This suggests that the polarization is predominantly a surface effect. This also agrees with the results of DFT calculations, which confirm that large surface dipoles can be induced by the addition of oxygen vacancies near the $SrTiO_{3-x}$ surface. Motion of these charged vacancies between the surface and sub-surface reverses the electric dipoles and explains the observed polarization dependence of the photocurrent. Overall, this work shows for the first time that oxygen vacancy-induced ferroelectricity in $SrTiO_{3-x}$ can improve photoelectrochemical energy to fuel conversion. Because the polarization affects only the materials surface, not the lattice, it preserves the high electric conductivity of the bulk. In contrast, charge transport in classic ferroelectric materials is slowed by the ferroelectric domain boundaries, which limits their photocurrent.[11] Also, oxygen vacancies are common among metal oxides, and therefore similar electric polarization effects are to be expected in other oxides. However, the limited stability of surface oxygen vacancies needs to be addressed before practical applications of the surface ferroelectric effect can be envisioned.

Experimental section

Double polished single crystals of strontium titanate with (111) facets and $10 \times 10 \times 0.5$ mm dimensions were purchased from MSE Supplies. Sodium sulfate (99.5%, Sigma Aldrich), potassium hexacyanoferrate (II) trihydrate (98.5–102.0%, Sigma-Aldrich), potassium ferricyanide (III) (99.9%, Fisher Chemical – Fisher Scientific), gallium indium eutectic (InGa, ≥99.99% trace metal basis, Aldrich Chemistry), gold coated glass (Thermo Scientific) were obtained from the respective sources. Water was purified to 18 MΩ cm resistivity using a nano-pure system.

Preparation of $SrTiO_{3-x}$

$SrTiO_{3-x}$ crystals were annealed in a ceramic boat inside of a quartz tube under 10% H_2: 90% Ar flowing gas (0.1 L min^{-1} : 0.9 L min^{-1}). The ramp rate was 50 °C/min and the single crystal was annealed at 1050 °C for 5 hours before cooling to room temperature naturally. The obtained $SrTiO_{3-x}$ crystals were grey in color.

Conclusion

In conclusion, we have shown that introduction of oxygen vacancies into strontium titanate single crystals with (111)

Electric polarization

The setup for the electric polarization of the single crystal is depicted in Fig. S1b. To prevent electric contact with gold substrates, Muscovite Mica sheets (25 × 25 mm, electron microscopy sciences, ≤65 μm thick each) were used as electrical insulation layer. The power supply input was set to 3.0 V and 130 mA, and a DC-HVDC Converter from the FS Series (XP Power) was employed to achieve an output voltage of approximately 545 V. The electrical bias was applied for 1 hour in either direction under a continuous argon flow of 1.0 L min^{-1} at room temperature. After polarization, samples were removed and characterized electrochemically within 1 hour.

Photoelectrochemistry measurement

Electrochemistry measurements were conducted using a Gamry Reference 600 Potentiostat connected to a three-electrode system. The system consisted of a GaIn-contacted SrTiO$_{3-x}$ single crystal working electrode with the backside covered by polyester masking tape (see Fig. S1a), a platinum counter electrode, and a calomel reference electrode (3.5 M KCl). Linear sweep voltammetry (LSV) was conducted in a quartz three-neck flask containing a 0.5 M Na$_2$SO$_4$ aqueous electrolyte solution (pH = 5.95). The LSV measurements were carried out under UV-light illumination from a 300 W Xe lamp source at an intensity of 60 mW cm^{-2} in air. Photoelectrochemical (PEC) scans were conducted under chopped illumination at a scan rate of 10 mV/s with a scan step of 1 mV, starting from negative to positive applied potential. The cell was calibrated using the half-wave potential of the [Fe(CN)$_6$]$^{3-/4-}$ redox couple, and potentials were then further converted from NHE to RHE, where RHE = NHE + (pH × 0.059 V). IPCE measurements were conducted with an applied bias of +1.23 V vs. RHE at pH = 5.95 and using a 375 nm LED light source operated at 17.0 V/240 mA. Mott–Schottky measurements were performed with a 10 mV rms AC voltage at variable frequency. These measurements were conducted in the dark using a sealed three-neck flask with constant nitrogen purging. The electrolyte used for Mott–Schottky measurements was K$_3$[Fe(CN)$_6$]/K$_4$[Fe(CN)$_6$]/(50 mM each). Contact with the working electrode for Mott–Schottky measurements was made using an InGa eutectic. The backside of the crystal was covered with polyester masking tape to prevent contact with the solution. After each Mott–Schottky measurement, residual InGa eutectic was removed by etching with concentrated HNO$_3$ for 20 s, followed by washing with water for 20 s and by drying in air.

Stability experiments

SrTiO$_3$ single crystal were stored either at ambient conditions or under argon gas flow (1.0 L min^{-1}). In both storage methods, the samples were protected from direct light exposure. After PEC measurements, samples were rinsed twice with deionized water and gently wiped with a kimwipe. They were then allowed to air dry for 5 minutes. For ambient condition storage, the single crystal was placed in a closed lid plastic container at room temperature. In the case of argon storage, the single crystal was placed on a ceramic boat crucible and stored in a tube under continuous argon flow at 1.0 L min^{-1}.

Surface photovoltage spectroscopy

SPS measurements were performed inside of a custom-made chamber that was purged with water-saturated N$_2$ gas at a rate of 1.0 L min^{-1} to prevent drying of the sample. The crystal was mounted underneath a vibrating gold mesh Kelvin probe (Delta PHI Besocke), as shown in Fig. S1c, and covered with deionized water (15 μL) and a microscopy glass cover slide. Illumination with monochromatic light (1–10 mW cm^{-2}) was provided from a 300 W Xe arc lamp after filtering through a monochromator (Oriel Cornerstone 130). Scans were conducted from 9600 to 40 000 cm^{-1} using 100 cm^{-1} steps every 5 seconds. Before illumination, samples were left to equilibrate until a stable contact potential difference (CPD) signal was obtained. The SPV data in Fig. 3b is relative to the dark, SPV = CPD(light) − CPD(dark).

X-ray photoelectron spectroscopy

XPS was conducted with a Kratos Supra XPS spectrometer equipped with a Al Kα source that generates X-rays at 1487 eV. All measurements were performed in the ultra-high vacuum (UHV) analytical chamber with the pressure of 10^{-7} mbar. The spectra were electrostatically corrected based on the position of C 1s (284.8 eV). STO single crystal pristine as bought or after H$_2$ annealed were surveyed for O 1s, Ti 2p, Sr 3d, and survey spectrum scan. Polarized samples were analyzed within 60 minutes after electric polarization.

Theoretical calculations

DFT+U calculations were carried out with the plane-waves pseudopotential method as implemented in the Quantum Espresso package.[75,76] All electronic structure and polarization calculations used generalized gradient approximation exchange and correlation functional by Perdew, Burke, Ernzerhof revised for solids (PBEsol),[77,78] and ultrasoft pseudopotentials with Sr (4s1 5s2 4p2 5p3), Ti (3s2 4s1 3p2 3d3), O (2s1 2p2) valence states.[78–80] Hubbard correction U = 4.57 eV was applied to Ti3d. The Atomic Simulation Environment (ASE)[76] was used to create a 3 × 3 × 3 symmetric SrO-terminated (111) slab using a SrTiO$_3$ unit cell with a vacuum layer of 20 Å separating the periodic images of the slab. The 3 × 3 model of the (111) surface unit cell is necessary to avoid interaction of vacancies with their periodic images. SrTiO$_3$ structures can be divided into 3 categories: pristine, surface oxygen vacancy (Vo) and subsurface Vo. 171 and 170 atoms comprise pristine and oxygen deficient structures respectively. Self-consistent field calculations and geometry relaxations are carried out integrating the Brillouin zone with a 2 × 2 × 1 uniform k-point mesh.'' Geometry optimization was performed on the pristine structure, the optimized pristine structure was then used as the starting point for the oxygen removal. A geometry optimization was performed for each charge state of the oxygen vacancy, freezing the positions of the atoms in the bottom 3 layers. Subsequently,

the Berry phase approach[81–84] was used to perform polarization calculations. The charge distribution was determined with Bader charge analysis.[85]

Author contributions

The experiments were designed by F. E. O and S. A and conducted by S. A. DFT calculations were performed by T. M. The manuscript was written by F. E. O. and S. A. with contributions by D. D. and T. M. All authors have given approval to the final version of the manuscript.

Conflicts of interest

There are no conflicts of interest to declare.

Data availability

Data in support of the conclusions of this study is presented in the manuscript and in the SI. Supplementary information: Schematics, photos, photoelectrochemical data, DOS diagrams, calculation details, and XPS data. See DOI: https://doi.org/10.1039/d5ey00266d.

Acknowledgements

References

1 J. Valasek, *Phys. Rev.*, 1921, **17**, 475–481.
2 K. T. Butler, J. M. Frost and A. Walsh, *Energy Environ. Sci.*, 2015, **8**, 838–848.
3 L. W. Martin and A. M. Rappe, *Nat. Rev. Mater.*, 2016, **2**, 16087.
4 M. Cain, *Characterisation of Ferroelectric Bulk Materials and Thin Films*, 2014.
5 P. Lopez-Varo, L. Bertoluzzi, J. Bisquert, M. Alexe, M. Coll, J. Huang, J. A. Jimenez-Tejada, T. Kirchartz, R. Nechache, F. Rosei and Y. Yuan, *Phys. Rep.*, 2016, **653**, 1–40.
6 G.-L. Yuan and J. Wang, *Appl. Phys. Lett.*, 2009, **95**, 252904.
7 S. Nishioka, F. E. Osterloh, X. Wang, T. E. Mallouk and K. Maeda, *Nat. Rev. Methods Primers*, 2023, **3**, 42.
8 J. L. Giocondi and G. S. Rohrer, *Chem. Mater.*, 2001, **13**, 241–242.
9 J. L. Giocondi and G. S. Rohrer, *J. Phys. Chem. B*, 2001, **105**, 8275–8277.
10 S. Y. Yang, L. W. Martin, S. J. Byrnes, T. E. Conry, S. R. Basu, D. Paran, L. Reichertz, J. Ihlefeld, C. Adamo, A. Melville, Y. H. Chu, C. H. Yang, J. L. Musfeldt, D. G. Schlom, J. W. Ager and R. Ramesh, *Appl. Phys. Lett.*, 2009, **95**, 062909.
11 S. Y. Yang, J. Seidel, S. J. Byrnes, P. Shafer, C. H. Yang, M. D. Rossell, P. Yu, Y. H. Chu, J. F. Scott, J. W. Ager, L. W. Martin and R. Ramesh, *Nat. Nanotechnol.*, 2010, **5**, 143–147.
12 S. Assavachin and F. E. Osterloh, *J. Am. Chem. Soc.*, 2023, **145**, 18825–18833.
13 M. R. Morris, S. R. Pendlebury, J. Hong, S. Dunn and J. R. Durrant, *Adv. Mater.*, 2016, **28**, 7123–7128.
14 Y. Liu, M. Zhang, Z. Wang, J. He, J. Zhang, S. Ye, X. Wang, D. Li, H. Yin, Q. Zhu, H. Jing, Y. Weng, F. Pan, R. Chen, C. Li and F. Fan, *Nat. Commun.*, 2022, **13**, 4245.
15 H. Magnan, P. M. Deleuze, J. Brehin, T. Plays, D. Stanescu, W. R. Flavell, M. G. Silly, B. Domenichini and A. Barbier, *J. Phys. Chem. C*, 2020, **124**, 10315–10323.
16 W. J. Merz, *Phys. Rev.*, 1954, **95**, 690–698.
17 W. J. Merz, *Phys. Rev.*, 1953, **91**, 513–517.
18 W. Käppler and G. Arlt, *Phys. Status Solidi (a)*, 1981, **63**, 475–480.
19 P. S. Brody, *Solid State Commun.*, 1973, **12**, 673–676.
20 M. Choi, F. Oba, Y. Kumagai and I. Tanaka, *Adv. Mater.*, 2013, **25**, 86–90.
21 Y. S. Kim, J. Kim, S. J. Moon, W. S. Choi, Y. J. Chang, J.-G. Yoon, J. Yu, J.-S. Chung and T. W. Noh, *Appl. Phys. Lett.*, 2009, **94**.
22 R. He, J. L. Lin, Q. Liu, Z. Liao, L. Shui, Z. J. Wang, Z. Zhong and R.-W. Li, *ACS Appl. Mater. Interfaces*, 2020, **12**, 45602–45610.
23 K. Klyukin and V. Alexandrov, *Phys. Rev. B*, 2017, **95**, 035301.
24 S. Suzuki, A. Honda, N. Iwaji, S. I. Higai, A. Ando, H. Takagi, H. Kasatani and K. Deguchi, *Phys. Rev. B: Condens. Matter Mater. Phys.*, 2012, **86**, 060102.
25 J. G. Bednorz and K. A. Müller, *Phys. Rev. Lett.*, 1984, **52**, 2289–2292.
26 A. Durán, E. Martínez, J. A. Díaz and J. M. Siqueiros, *J. Appl. Phys.*, 2005, **97**, 104109.
27 A. S. Kumar, P. Suresh, M. M. Kumar, H. Srikanth, M. L. Post, S. Kathy, M. Ralf and S. Srinath, *J. Phys.: Conf. Ser.*, 2010, **200**, 092010.
28 S. Assavachin, B. A. Nail, R. V. Goncalves, J. R. Mulcahy, S. E. Lloyd and F. E. Osterloh, *Mater. Adv.*, 2020, **1**, 1382–1389.
29 R. Munprom, P. A. Salvador and G. S. Rohrer, *J. Mater. Chem. A*, 2016, **4**, 2951–2959.
30 Y. S. Kim, J. S. Choi, J. Kim, S. J. Moon, B. H. Park, J. Yu, J.-H. Kwon, M. Kim, J.-S. Chung, T. W. Noh and J.-G. Yoon, *Appl. Phys. Lett.*, 2010, **97**, 242907.
31 J. H. Haeni, P. Irvin, W. Chang, R. Uecker, P. Reiche, Y. L. Li, S. Choudhury, W. Tian, M. E. Hawley, B. Craigo,

A. K. Tagantsev, X. Q. Pan, S. K. Streiffer, L. Q. Chen, S. W. Kirchoefer, J. Levy and D. G. Schlom, *Nature*, 2004, **430**, 758.

32 D. Lee, S. H. Baek, T. H. Kim, J. G. Yoon, C. M. Folkman, C. B. Eom and T. W. Noh, *Phys. Rev. B: Condens. Matter Mater. Phys.*, 2011, **84**, 125305.

33 C. H. Ahn, K. M. Rabe and J.-M. Triscone, *Science*, 2004, **303**, 488–491.

34 J. G. Mavroides, J. A. Kafalas and D. F. Kolesar, *Appl. Phys. Lett.*, 1976, **28**, 241–243.

35 T. Takata and K. Domen, *J. Phys. Chem. C*, 2009, **113**, 19386–19388.

36 F. A. Kröger and H. J. Vink, in *Solid State Physics*, ed. F. Seitz and D. Turnbull, Academic Press, 1956, vol. 3, pp. 307–435.

37 R. Krol, *Photoelectrochemical Hydrogen Production*, 2012, vol. 102, pp. 13–67.

38 R. L. Wild, E. M. Rockar and J. C. Smith, *Phys. Rev. B: Condens. Matter Mater. Phys.*, 1973, **8**, 3828–3835.

39 V. M. Khomenko, K. Langer, H. Rager and A. Fett, *Phys. Chem. Miner.*, 1998, **25**, 338–346.

40 B. Jalan, R. Engel-Herbert, T. E. Mates and S. Stemmer, *Appl. Phys. Lett.*, 2008, 93.

41 H. Tan, Z. Zhao, W.-B. Zhu, E. N. Coker, B. Li, M. Zheng, W. Yu, H. Fan and Z. Sun, *ACS Appl. Mater. Interfaces*, 2014, **6**, 19184–19190.

42 S. Nishioka, J. Hyodo, J. J. M. Vequizo, S. Yamashita, H. Kumagai, K. Kimoto, A. Yamakata, Y. Yamazaki and K. Maeda, *ACS Catal.*, 2018, 7190–7200.

43 S. Ferrer and G. A. Somorjai, *Surf. Sci.*, 1980, **94**, 41–56.

44 D. A. Muller, N. Nakagawa, A. Ohtomo, J. L. Grazul and H. Y. Hwang, *Nature*, 2004, **430**, 657–661.

45 H. Yamada and G. R. Miller, *J. Solid State Chem.*, 1973, **6**, 169–177.

46 M. S. Wrighton, A. B. Ellis, P. T. Wolczanski, D. L. Morse, H. B. Abrahamson and D. S. Ginley, *J. Am. Chem. Soc.*, 1976, **98**, 2774–2779.

47 Z. Zhao, R. V. Goncalves, S. K. Barman, E. J. Willard, E. Byle, R. Perry, Z. Wu, M. N. Huda, A. J. Moulé and F. E. Osterloh, *Energy Environ. Sci.*, 2019, **12**, 1385–1395.

48 T. Takata, J. Jiang, Y. Sakata, M. Nakabayashi, N. Shibata, V. Nandal, K. Seki, T. Hisatomi and K. Domen, *Nature*, 2020, **581**, 411–414.

49 A. Kumar, P. G. Santangelo and N. S. Lewis, *J. Phys. Chem.*, 1992, **96**, 834–842.

50 Y. Cheng, C. Xiao, B. Mahmoudi, R. Scheer, A. W. Maijenburg and F. E. Osterloh, *EES Catal.*, 2023, **1**, 74–83.

51 S. Daemi, A. Kundmann, P. Cendula, K. Becker and F. E. Osterloh, *Energy Environ. Sci.*, 2023, **16**, 4530–4538.

52 R. Chen, F. Fan, T. Dittrich and C. Li, *Chem. Soc. Rev.*, 2018, **47**, 8238–8262.

53 J. M. Bolts and M. S. Wrighton, *J. Phys. Chem. C*, 1976, **80**, 2641–2645.

54 B. M. Klahr and T. W. Hamann, *J. Phys. Chem. C*, 2011, **115**, 8393–8399.

55 R. M. Doughty, B. Hodges, J. Dominguez, R. Han, Z. Zhao, S. Assavachin and F. E. Osterloh, *J. Phys. Chem. C*, 2020, **124**, 18426–18435.

56 K. Xie, N. Umezawa, N. Zhang, P. Reunchan, Y. Zhang and J. Ye, *Energy Environ. Sci.*, 2011, **4**, 4211–4219.

57 C. Wang, P. Koirala, P. Stair and L. Marks, *Appl. Surf. Sci.*, 2017, **422**, 661–665.

58 D. Hrabovsky, B. Berini, A. Fouchet, D. Aureau, N. Keller, A. Etcheberry and Y. Dumont, *Appl. Surf. Sci.*, 2016, **367**, 307–311.

59 R. P. Vasquez, *Surf. Sci. Spectra*, 1992, **1**, 129–135.

60 H. Chen, F. Zhang, W. Zhang, Y. Du and G. Li, *Appl. Phys. Lett.*, 2018, 112.

61 B. Kayaalp, K. Klauke, M. Biesuz, A. Iannaci, V. M. Sglavo, M. D'Arienzo, H. Noei, S. Lee, W. Jung and S. Mascotto, *J. Phys. Chem. C*, 2019, **123**, 16883–16892.

62 V. I. Anisimov, J. Zaanen and O. K. Andersen, *Phys. Rev. B: Condens. Matter Mater. Phys.*, 1991, **44**, 943–954.

63 W. E. Pickett, S. C. Erwin and E. C. Ethridge, *Phys. Rev. B: Condens. Matter Mater. Phys.*, 1998, **58**, 1201–1209.

64 M. Schmidbauer, A. Kwasniewski and J. Schwarzkopf, *Acta Crystallogr., Sect. B*, 2012, **68**, 8–14.

65 Y. Liang, W. Li, S. Zhang, C. Lin, C. Li, Y. Yao, Y. Li, H. Yang and J. Guo, *Sci. Rep.*, 2015, **5**, 10634.

66 N. Q. Minh, *J. Am. Ceram. Soc.*, 1993, **76**, 563–588.

67 V. Alexandrov, S. Piskunov, Y. F. Zhukovskii, E. A. Kotomin and J. Maier, *Integr. Ferroelectr.*, 2011, **123**, 10–17.

68 Y. Guo, B. Guo, W. Dong, H. Li and H. Liu, *Nanotechnology*, 2013, **24**, 275201.

69 R. Moubah, O. Rousseau, D. Colson, A. Artemenko, M. Maglione and M. Viret, *Adv. Funct. Mater.*, 2012, **22**, 4814–4818.

70 H. Liu, Y. Peng, G. Han, Y. Liu, N. Zhong, C. Duan and Y. Hao, *Nanoscale Res. Lett.*, 2020, **15**, 120.

71 T. Wan, B. Qu, H. Du, X. Lin, P. Guan, Q. Lin, N. Chen, T. Teck Tan, T. Hang and D. Chu, *J. Colloid Interface Sci.*, 2017, **494**, 178–184.

72 W. Jiang, M. Noman, Y. M. Lu, J. A. Bain, P. A. Salvador and M. Skowronski, *J. Appl. Phys.*, 2011, 110.

73 S. Das, B. Wang, Y. Cao, M. Rae Cho, Y. Jae Shin, S. Mo Yang, L. Wang, M. Kim, S. V. Kalinin, L.-Q. Chen and T. W. Noh, *Nat. Commun.*, 2017, **8**, 615.

74 W.-M. Zhong, X.-G. Tang, Q.-X. Liu, Y.-P. Jiang, W.-H. Li and J.-L. Yue, *Phys. B: Condens. Matter*, 2021, **615**, 413080.

75 P. Giannozzi, S. Baroni, N. Bonini, M. Calandra, R. Car, C. Cavazzoni, D. Ceresoli, G. L. Chiarotti, M. Cococcioni, I. Dabo, A. Dal Corso, S. de Gironcoli, S. Fabris, G. Fratesi, R. Gebauer, U. Gerstmann, C. Gougoussis, A. Kokalj, M. Lazzeri, L. Martin-Samos, N. Marzari, F. Mauri, R. Mazzarello, S. Paolini, A. Pasquarello, L. Paulatto, C. Sbraccia, S. Scandolo, G. Sclauzero, A. P. Seitsonen, A. Smogunov, P. Umari and R. M. Wentzcovitch, *J. Phys.: Condens. Matter*, 2009, **21**, 395502.

76 P. Giannozzi, O. Andreussi, T. Brumme, O. Bunau, M. Buongiorno Nardelli, M. Calandra, R. Car, C. Cavazzoni, D. Ceresoli, M. Cococcioni, N. Colonna,

I. Carnimeo, A. Dal Corso, S. de Gironcoli, P. Delugas, R. A. DiStasio, A. Ferretti, A. Floris, G. Fratesi, G. Fugallo, R. Gebauer, U. Gerstmann, F. Giustino, T. Gorni, J. Jia, M. Kawamura, H. Y. Ko, A. Kokalj, E. Küçükbenli, M. Lazzeri, M. Marsili, N. Marzari, F. Mauri, N. L. Nguyen, H. V. Nguyen, A. Otero-de-la-Roza, L. Paulatto, S. Poncé, D. Rocca, R. Sabatini, B. Santra, M. Schlipf, A. P. Seitsonen, A. Smogunov, I. Timrov, T. Thonhauser, P. Umari, N. Vast, X. Wu and S. Baroni, *J. Phys.: Condens. Matter*, 2017, **29**, 465901.

77 J. P. Perdew, A. Ruzsinszky, G. I. Csonka, O. A. Vydrov, G. E. Scuseria, L. A. Constantin, X. Zhou and K. Burke, *Phys. Rev. Lett.*, 2008, **100**, 136406.

78 G. Kresse and D. Joubert, *Phys. Rev. B: Condens. Matter Mater. Phys.*, 1999, **59**, 1758–1775.

79 B. J. Austin, V. Heine and L. J. Sham, *Phys. Rev.*, 1962, **127**, 276–282.

80 V. Heine, in *Solid State Physics*, eds. H. Ehrenreich, F. Seitz and D. Turnbull, Academic Press, 1970, vol. 24, pp. 1–36.

81 R. Resta, *Ferroelectrics*, 1994, **151**, 49–58.

82 R. Resta, *Rev. Mod. Phys.*, 1994, **66**, 899–915.

83 R. M. Martin, *Phys. Rev. B: Condens. Matter Mater. Phys.*, 1972, **5**, 1607–1613.

84 R. Resta, *Ferroelectrics*, 1992, **136**, 51–55.

85 G. Henkelman, A. Arnaldsson and H. Jónsson, *Comput. Mater. Sci.*, 2006, **36**, 354–360.